

Supporting Information

Experimental Demonstration of an Electride as a 2D Material

Daniel L. Druffel,[†] Kaci L. Kuntz,[†] Adam H. Woomer,[†] Francis M. Alcorn,[†] Jun Hu,[†] Carrie L. Donley,[§] and Scott C. Warren^{†§}*

[†] Department of Chemistry and [§] Department of Applied Physical Sciences, University of North Carolina at Chapel Hill, Chapel Hill, North Carolina 27599, United States.

*Email: sw@unc.edu

Contents

1.	3D Ca ₂ N synthesis and characterization	2
2.	DFT calculations of Ca ₂ N and graphite	3
3.	Screening solvents for liquid exfoliation of Ca ₂ N	4
4.	Transmission electron microscopy experiments and simulations	6
5.	Calcium and nitrogen assays	8
6.	Photoemission	9
7.	Optical response of 2D Ca ₂ N	11
8.	Supporting References	16

1. 3D Ca₂N Synthesis and Characterization

3D Ca₂N was synthesized by the reduction of Ca₃N₂ (Alfa Aesar, 99%) with Ca metal (Alfa Aesar, redistilled granules ~16 mesh, 99.5%) as adapted from previous literature.^{1,2} The Ca₃N₂ was ground into a very fine powder and Ca granules were added. The mixture was ground lightly together in a 1.02:1 Ca:Ca₃N₂ molar ratio (total mass of a typical batch: 1.2 g) and pressed into a pellet under ~0.56 GPa of pressure using a hydraulic press. The pellet, along with an additional ~0.600 g of Ca metal, was placed into a pocket of Mo foil (Alfa Aesar 99.95%), which was subsequently crimped closed. The Mo pocket was then sealed inside an evacuated (4×10^{-3} mbar) quartz ampoule (18 mm ID, ~6-7 cm in length). The ampoule was heated in a Lindberg Blue tube furnace to 1100 K at a ramp rate of 100K/hr. The temperature was held at 1100 K for 2 days and cooled to room temperature over 24 hours. The additional calcium metal that was added inside of the Mo pocket reacted with the quartz ampoule covering the ampoule wall in shiny black/grey material. We found that adding Ca helped prevent the loss of Ca from the pellet. The obtained Ca₂N pellet was black. When broken apart, the material was black and shiny with a blue luster. All materials were stored in a glovebox with a nitrogen atmosphere (oxygen < 0.01 ppm) and all synthetic steps were carried out under nitrogen atmosphere.

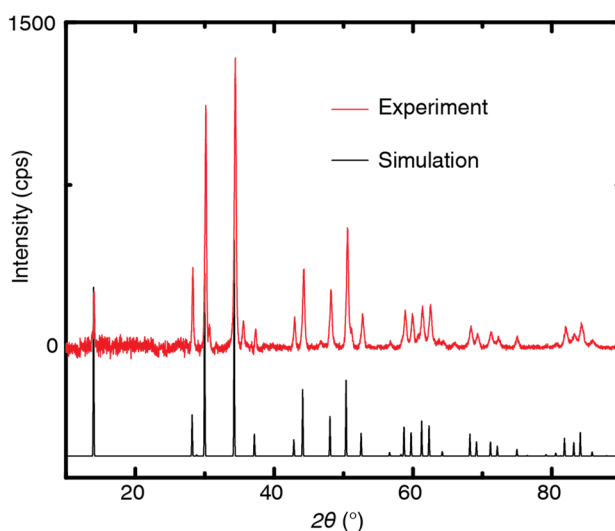


Figure S1. Powder X-ray diffraction pattern of synthesized Ca₂N compared to a simulation of the diffraction pattern using reported crystal parameters.³

To acquire an X-ray diffraction pattern of Ca₂N (Figure S1), the powder was ground very finely, deposited on a roughened glass slide, and covered with 1 mil Kapton tape while in the glovebox to prevent oxidation during the measurement. The measurement was taken using a Rigaku Multiflex X-ray diffractometer with a CuK α X-ray source. We compared our crystal to previous literature³ and found excellent agreement with the reported hexagonal crystal system, $R\bar{3}m$ space group, and lattice parameters $a = 3.624$ $c = 19.100$ Å. The Kapton tape has a broad signal from 10-26°, which reduces the relative intensity of the 003 peak and increases the noise in that region. We note that there are small peaks at 30.6° and 35.7° that we could not assign to a

plane in the Ca₂N crystal. We attribute those peaks to an unidentified contaminant phase present in many of our samples.

2. DFT Calculations of Ca₂N and graphite

Density functional theory (DFT) calculations were performed using the CASTEP⁴ code with plane-wave basis set⁵ approximations. Ultrasoft⁶ pseudopotentials were used to describe core electrons, and a 400 eV cut-off energy was used. For this cut-off energy, calculations were convergent with dE/dE_{cut} less than 0.01 meV/atom. A GGA PBE functional⁷ was used for the exchange-correlation contribution to total energy and Grimme's DFT-D⁸ correction was used to account for long-range dispersion forces. Both graphite and bulk Ca₂N were structurally relaxed prior to further calculations. A Monkhorst-Pack⁹ grid of 8x8x2 k-points was used for the geometry optimization and interlayer binding energy study. Each crystal structure relaxed to within 2% of experimentally determined parameters.

To determine binding energy for both graphite and Ca₂N, we varied the interlayer distance between layers in each crystal structure and then calculated the total energy. An 'infinite' structure was built with an interlayer distance of 12 Å, such that there were no interactions between sheets. We then calculated the interlayer binding energy as either $(E-E_{\infty})/(\# \text{ of atoms at interface})$ or $(E-E_{\infty})/(\# \text{ of interfaces} \times \text{area})$.

For electronic structure calculations, we used a denser MK grid, of 64x64x10 and 64x64x64 for the hexagonal and rhombohedral orientations of Ca₂N. The bandstructure of rhombohedral Ca₂N shown in Figure 4e agrees with previously reported calculations¹ and experimentally determined band structures.¹⁰ The integrated electron density was within 0.0001 e⁻ of the total electron count, and thus we assume all electrons were accounted for and our mesh was sufficient to accurately describe electron density.

The joint density of states (JDOS) was calculated from the CASTEP output with OptaDOS code¹¹⁻¹³ using a Gaussian broadening scheme with a 0.05 eV smearing width. To image the orbital projections of valence and conduction band states, we used the STM profile module of CASTEP for a given negative or positive bias, respectively. Specifically, an applied bias of -1.49 eV was used to image the interlayer electron gas of bulk Ca₂N. To obtain the electron density profile, we used Perl scripting to extract and integrate total electron count across the *z*-axis of the hexagonal unit cell.

The band structure of Ca₂N changes subtly with thickness (Figure S2a,f) in agreement with other reports¹⁴ and does not change with lateral interlayer translation.¹⁵ Therefore, we expect the band structure of our few-layer flakes to be similar to that of the 3D solid, which was recently shown by angle-resolved photoemission spectroscopy to match the DFT predictions.¹⁰

Images of the orbital projections for monolayer Ca₂N show that both of the bands that cross the Fermi level contribute to the electron density covering the monolayer's surface (Figure S2b,c,d) in agreement with previous findings.^{14,16} The electron gas extends as far as 2.0 Å from the calcium atoms of the monolayer. Images of the orbital projections for bilayer Ca₂N show that the electron gas sandwiched between layers is at a slightly lower energy than the electron gas at the surface (Figure S2g,j) and that the electron gas at the surface consists largely of filled states in the energy range -0.56 eV to E_F (Figure S2i,j).

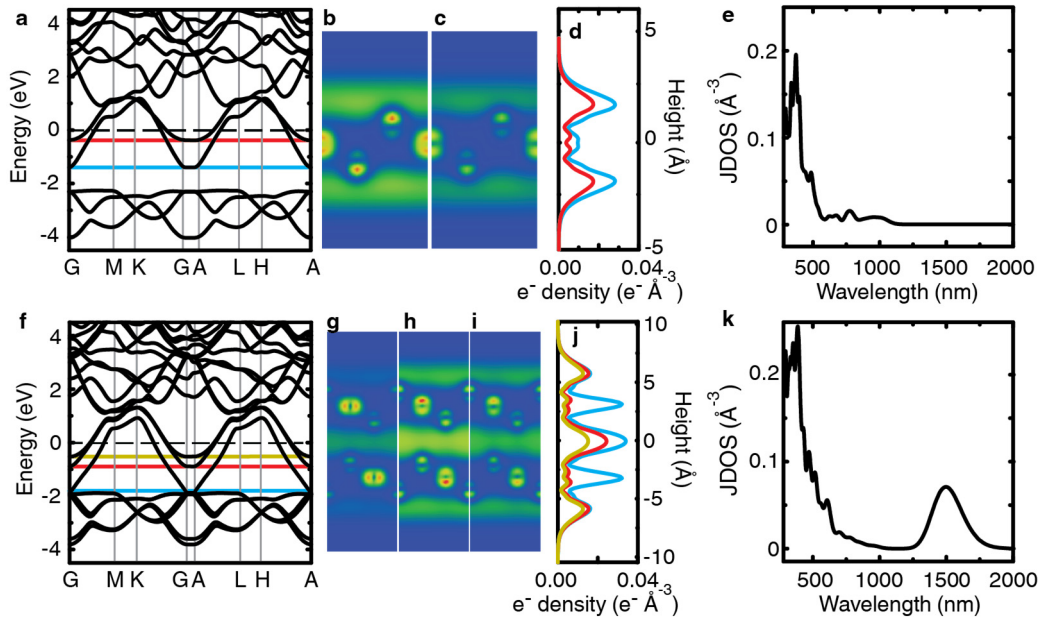


Figure S2. Electronic structure of mono- and bilayer Ca_2N . a) Band structure of monolayer Ca_2N calculated from the hexagonal unit cell. Projections of the integrated electron density of monolayer Ca_2N within the unit cell as calculated by density functional theory (DFT). The integration is over states in the energy range b) -1.41 eV (blue line) to E_F and c) -0.39 eV (red line) to E_F . The color gradient in b and c ranges from an electron density of 0.00 (blue) to $0.10 \times 10^{-3} \text{ e}^- \text{ \AA}^{-3}$ (red). d) The electron density profile integrated along the z -axis of the unit cell for the states in b and c. e) The joint density of states (JDOS) for monolayer Ca_2N . f) Band structure of bilayer Ca_2N calculated from the hexagonal unit cell. Projections of the electron density of bilayer Ca_2N integrated over states in the energy range g) -1.88 eV (blue line) to E_F , h) -0.90 eV (red line) to E_F , and i) -0.56 eV (yellow line) to E_F . The color gradient (blue to red) in g, h, and i varies from 0.00 to $0.41 \times 10^{-3} \text{ e}^- \text{ \AA}^{-3}$, 0.00 to $0.14 \times 10^{-3} \text{ e}^- \text{ \AA}^{-3}$, and 0.00 to $0.14 \times 10^{-3} \text{ e}^- \text{ \AA}^{-3}$, respectively. j) The electron density profile integrated along the z -axis of the unit cell for the states in g, h and i. k) The JDOS for bilayer Ca_2N .

The JDOS for the bilayer has a distinct peak at 1500 nm (Figure S2), which arises from direct transitions from the lowest of the three bands crossing the Fermi level to either of the top two bands crossing the Fermi level. These bands are split by ~ 0.83 eV because of the coupling between the electron layers.¹⁴ The top two bands are primarily composed of states in which the electron density resides on the outer-most electron layer, while the lowest of the three bands is composed of states in which the electron density is sandwiched in between planes of $[\text{Ca}_2\text{N}]^+$.

3. Screening solvents for liquid exfoliation of Ca_2N

All solvents were purchased from Sigma Aldrich and dried with 4\AA molecular sieves unless otherwise noted. The solvents included: 1,3-dioxolane (anhydrous, 99.5%), dimethyl carbonate (anhydrous, $\geq 99\%$), dimethoxy ethane (anhydrous, 99.5%), toluene (Fisher 99.9%), hexane (Fisher 99.9%), benzene ($\geq 99.9\%$), benzyl benzoate ($\geq 99.0\%$), ethyl acetate (Fisher, 99.9%), *N*-methyl-2-pyrrolidone (anhydrous, 99.5%), 1-vinyl-2-pyrrolidinone ($\geq 99\%$), 1-octyl-2-pyrrolidone ($\geq 98\%$), 1,3-dimethyl-2-imidazolidinone ($\geq 99\%$), *N*-dodecyl-2-pyrrolidinone ($\geq 99\%$), benzyl ether ($\geq 98\%$), dimethylsulfoxide ($\geq 99.9\%$), chlorobenzene ($\geq 99.5\%$), dichlorobenzene ($\geq 99.5\%$),

1,2,4-trichlorobenzene ($\geq 99.5\%$), cyclohexanone ($\geq 99.8\%$), benzaldehyde ($\geq 99\%$), triethylamine ($\geq 99\%$), diethyl ether (Fisher, 99.9%), tetrahydrofuran (anhydrous, 99.8%), 1,4-dioxane (anhydrous, 99.8%), dimethylformamide ($\geq 99\%$), dichloromethane (Fisher, 99.9%), acetonitrile (Acros, anhydrous, 99.9%), acetone (Fisher, 99.9%), and *N*-methylformamide ($\geq 99\%$).

Working in a glovebox, we suspended bulk Ca_2N powder (10 mg) in each solvent (20 mL) and sealed the suspensions in polypropylene-capped vials with additional parafilm and Teflon tape wrapped around the lid. We sonicated the sealed suspensions for 100 minutes in a water sonication bath outside of the glovebox with the temperature of the bath below 34 °C.

Table S1. Solvents screened for liquid exfoliation of Ca_2N . Ca_2N in compatible solvents (listed in green) remained black after several days and remained suspended. Ca_2N in non-reactive solvents (listed in grey) remained black after several days and precipitated rapidly. Ca_2N in slightly reactive solvents (listed in light yellow) decomposed to a white powder after 5-10 days. Ca_2N in reactive solvents (listed in yellow) decomposed to a white powder after 24-72 hours. Ca_2N in very reactive solvents (listed in red) decomposed to a white powder and produced bubbles within minutes.

1,3-dioxolane
Dimethyl carbonate
Dimethoxy ethane
Toluene
Hexane
Benzene
Benzyl Benzoate
<i>N</i> -Methyl-2-pyrrolidone
1-Octyl-2-pyrrolidone
<i>N</i> -Vinylpyrrolidone
1,3-Dimethyl-2-imidazolidinone
<i>N</i> -Dodecyl-2-pyrrolidone
Ethyl acetate
Benzyl ether
Dimethyl sulfoxide
Chlorobenzene
Dichlorobenzene
1,2,4-trichlorobenzene
Cyclohexanone
Benzaldehyde
Triethylamine
Diethyl ether
Tetrahydrofuran
1,4-dioxane
Dimethylformamide
Dichloromethane
Acetonitrile
Chloroform
Acetone
<i>N</i> -Methylformamide

After identifying 1,3-dioxolane as the most promising solvent, we repeated the screening with 1,3-dioxolane, tetrahydrofuran (THF), and 1,4-dioxane, which have similar structures. Ca_2N (10 mg) decomposed to a white powder after 24-72 hours of exposure to THF or 1,4-dioxane. To ensure that the solvents had very minimal water content and to remove stabilizers, we dried each solvent over sodium metal and distilled the dry solvent over a Schlenk line with N_2 environment. The repeated screening yielded the same results; Ca_2N (10 mg) decomposed to a white powder after 24-72 hours of exposure to THF or 1,4-dioxane. The X-ray diffraction pattern of the white powder matches that of $\text{Ca}(\text{OH})_2$ (Figure S3).

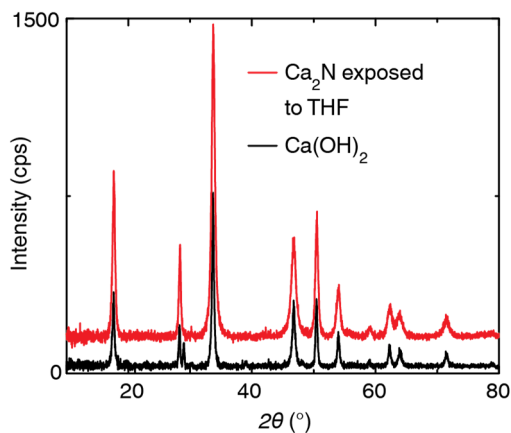


Figure S3. Powder X-ray diffraction pattern of $\text{Ca}(\text{OH})_2$ and Ca_2N exposed to THF for 24 hours.

In all subsequent experiments, 1,3-dioxolane was dried over sodium and distilled just before use.

4. Transmission Electron Microscopy Experiments and Simulations

In a typical experiment, Ca_2N powder was suspended in 1,3-dioxolane (2.5 mg/mL) as described above and was sonicated for 800 minutes under anhydrous and oxygen-free conditions. The suspension was centrifuged at 300 rpm for 15 min to isolate the exfoliated material. Several microliters of the suspension were drop-cast onto a lacey carbon grid and dried in a vacuum chamber for 30 minutes. The samples were loaded into a high-resolution transmission electron microscope (HR-TEM) using a nitrogen-filled glovebag to minimize exposure to air and water.

To obtain selected area diffraction patterns, the samples were loaded into a low resolution TEM following the same procedure as above. TEM images show that the materials are thin and flat though there is a distribution of flake thicknesses and sizes (Figure S4). Some material is non-sheet-like or appears to be an aggregate of sheets despite our attempt to isolate the thinnest materials.

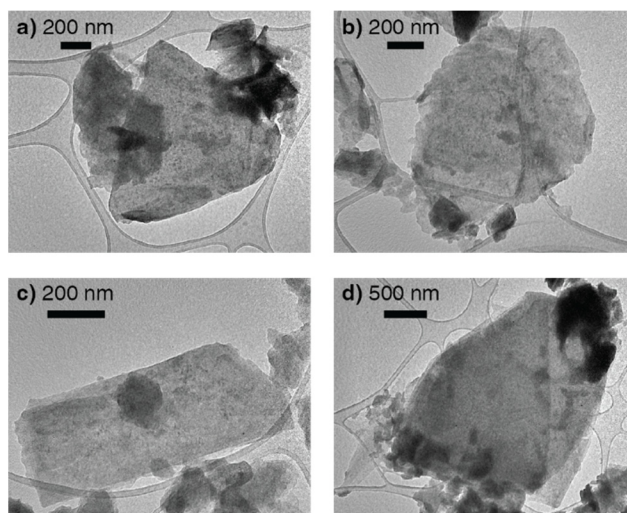


Figure S4. Low-resolution transmission electron microscopy images of flakes of 2D Ca_2N .

We simulated the selected area diffraction pattern by multislice calculations (JEMS).¹⁷ To understand the effect of flake thickness on the diffraction pattern, we modeled crystal structures of Ca_2N with thicknesses of 1-8 layers. The monolayer (Figure S5a) shows two sets of hexagonal diffraction spots with d-spacing 1.80 and 3.12 Å, in agreement with our experimental measurements. For flakes thicker than a bilayer, the intensity of the spot corresponding to the larger d-spacing is negligible.

The effect of translational disorder was examined by modeling various stacking configurations of Ca_2N . The material is expected to have an ABC stacking sequence in the three layers in the unit cell, but the energetic cost of translating layers is low. We modeled alternate stacking sequences, including ABAC, ABAB, ACAC, ABC-ABC-ABA-ABC-ABC, ACC-ACC-ABA-CBB-BAB. For example, in the sequence ABC-ABC-ABA-ABC-ABC the ninth “C” plane has been replaced with an “A” plane, which is equivalent to translating that “C” plane by 2.09 Å in the direction perpendicular to the X-axis. In the translated structures, like the ABC-ABC-ABA-ABC-ABC stacking sequence (Figure S5c), both sets of diffraction spots are present. The intensity of the spots varies significantly with the stacking sequence. For example, in the highly disordered sequence ACC-ACC-ABA-CBB-BAB (Figure S5d), the diffraction spots of the larger d-spacing (3.12 Å) are more intense than the spots at the smaller d-spacing (1.80 Å).

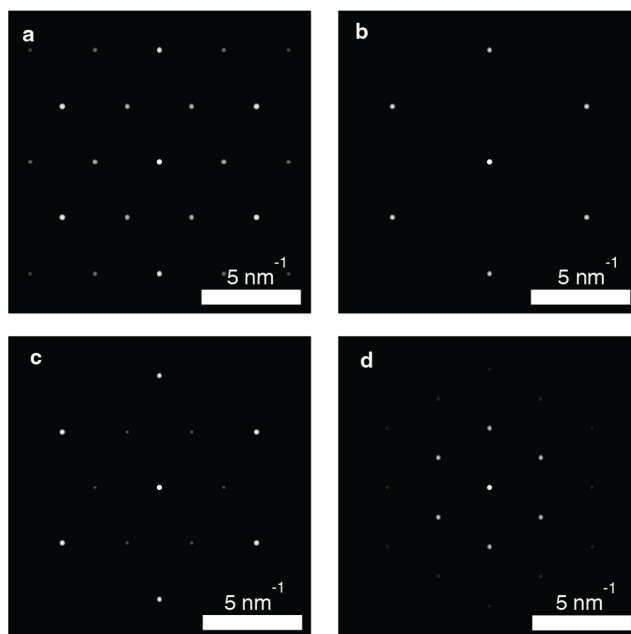


Figure S5. Simulated diffraction pattern of a) monolayer Ca_2N , b) trilayer Ca_2N , c) Ca_2N with stacking sequence ABC-ABC-ABA-ABC-ABC, d) Ca_2N with stacking sequence ACC-ACC-ABA-CBB-BAB looking down the [001] zone axis.

5. Calcium and Nitrogen Assays

We measured the calcium and nitrogen content of metal nitrides. To determine the concentration of calcium, we titrated Ca^{2+} with ethylenediaminetetraacetic acid (EDTA, Sigma Aldrich, 99%) in the presence of the indicator carconcarboxylic acid (Alfa Aesar, used-as-recieved).¹⁸ First, under nitrogen atmosphere, we digested the samples into $(\text{NH}_4)_2\text{SO}_4$ and $\text{Ca}(\text{OH})_2$ by injecting 1 M H_2SO_4 (Fischer, Trace Metal Grade). Then the digested samples were diluted in deionized water to a measurable concentration (about 1.5 mM). The pH of the titrand was kept basic by the addition of NaOH (0.583 M final concentration), which we prepared from NaOH pellets (Fischer, NF/FCC) and deionized water. A stock solution of indicator was prepared fresh for each trial by dissolving carconcarboxylic acid (0.168 mM final concentration) in a 50/50 v/v water-isopropyl alcohol mixture, which was added to the titrand. Sodium potassium tartrate (Sigma Aldrich, $\geq 99\%$, 0.0202 M final concentration) was also added to the titrand. The solution was titrated with 0.1202 mM EDTA. Each measurement was repeated ten times.

To measure the amount of nitrogen, we used the Berthelot reaction,¹⁹ a stoichiometric reaction between ammonia and phenol that yields a blue indophenol dye, the concentration of which is quantified by spectroscopy. We digested the samples of metal nitrides into $(\text{NH}_4)_2\text{SO}_4$ and $\text{Ca}(\text{OH})_2$ by injecting 1 M H_2SO_4 (Fischer, Trace Metal Grade). Standards (1.860 to 753.2 μM) of $(\text{NH}_4)_2\text{SO}_4$ (Alfa Aesar, $>99\%$) with $\text{Ca}(\text{OH})_2$ (Fischer, Certified) in a 1:1 ratio were prepared in deionized water and stored in a refrigerator. To the samples and standards, solutions of EDTA (final concentration 0.003479 M), phenol (Alfa Aesar, 99%, unstabilized, 0.06345 M final

concentration), sodium nitroprusside (Alfa Aesar, 99%, 0.09375 mM final concentration), Na₂HPO₄ (Sigma Aldrich, 99.95%, final concentration 0.9099 mM), NaOCl (Sigma Aldrich, reagent grade, available chlorine 4.00-4.99%, final concentration 0.03885 M), and NaOH (Fischer, NF/FCC, final concentration 0.1610 M) were added. The combined solutions were incubated for 50 minutes to develop color. Then the solution was pipetted into a glass cuvette and measured using a Cary 5000 double-beam spectrometer using 450-800 nm wavelength light. The indophenol dye has a $\lambda_{\text{max}} = 640$ nm. Each measurement was repeated ten times.

We confirm the applicability of this approach to metal nitrides by measuring the stoichiometry of Ca₃N₂ (Alfa Aesar, 99%) as Ca₃N_{2.02±0.03}. In addition, both the calcium and nitrogen assays gave molar concentrations that match the expected amount of sample digested. For example, a sample (19.1 ± 1 mg) of Ca₃N₂, which was expected to contain 384 ± 20 μmol of calcium and 256 ± 10 μmol of nitrogen, was measured to contain 384 ± 5 μmol of calcium and 260 ± 4 μmol of nitrogen. Therefore, in addition to an accurate stoichiometry, this method can be used to measure the concentration of unknown masses of metal nitrides, which we used to measure the concentration of our 2D Ca₂N suspended in 1,3-dioxolane.

6. Photoemission

X-ray photoemission spectroscopy (XPS) was used to investigate the surface of 2D Ca₂N, 3D Ca₂N, Ca₃N₂, oxidized Ca₂N, and Ca(OH)₂. Suspensions of 2D Ca₂N in 1,3-dioxolane were drop-cast onto a p-doped silicon wafer with a thick thermal oxide (300nm) under inert atmosphere (N₂, <0.01ppm O₂, <0.01ppm H₂O). The wafer was heated to 75 °C for 15 min and subsequently dried under low vacuum for 15 min to drive off 1,3-dioxolane. Ca₃N₂, Ca(OH)₂, and oxidized Ca₂N (exposed to ambient conditions for two weeks) were each imbedded into indium foil under inert atmosphere. The samples were then loaded into a Kratos Axis Ultra Delay-Line Detector (DLD) spectrometer under dry N₂ conditions and held under a high vacuum (<10⁻⁹ torr) for analysis. The oxide species were loaded into the XPS instrument separately from air-sensitive samples. The X-ray source was a monochromatic Al K α source (1487.7 eV). A charge neutralizer (1.8 A filament current, 2.8 V charge balance, 0.8 V filament bias) was used with all oxide species; air-sensitive species were investigated with and without the charge neutralizer. The spectra were corrected to the carbon 1s peak for adventitious carbon (284.6 eV).²⁰

By comparing the area of the peaks of the Ca 2p core electrons to N 1s core electrons and accounting for the atomic sensitivity factors, we measured the ratio of Ca:N for 2D Ca₂N (5.3:1), Ca₃N₂ (4.6:1), and oxidized Ca₂N (18:1). We found that the ratio is significantly calcium-rich in all measurements and the intensity of the nitrogen peak is low in all samples.

We noticed a trend in the C 1s spectra that the area of the peak at ~289.5 eV increases relative to the area of the peak at 284.6 eV for oxidized 2D Ca₂N relative to unoxidized Ca₂N (Figure S6). This was observed in all samples and may be indicative of CaCO₃ or other C=O bond formation.

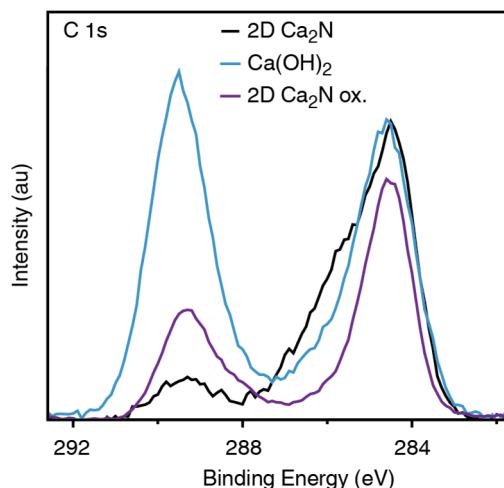


Figure S6. XPS spectra of core C 1s electrons for 2D Ca₂N, deliberately oxidized 2D Ca₂N, and Ca(OH)₂.

Ultraviolet photoemission spectroscopy (UPS) provides information about the valence band of the material and the density of states near the Fermi energy edge. For UPS studies, 2D Ca₂N samples were drop-cast onto metal-plated silicon wafers (5 nm adhesive metal, either Cr or Ti, and 50 nm of conductive metal, either Au or Pt). Samples were prepared in the same manner as for XPS analysis described above. A He I source (21.2 eV) was used for UPS measurements.

In order to measure the metallic character of Ca₂N and not the substrate, we cast films much thicker than the escape depth of electrons. We characterized the films by XPS and then cleaned the surface of the films by argon ion sputtering. The quality of substrate coverage by Ca₂N was assessed by measuring the area of peaks from Pt or Au. We performed sputtering twice for 15 minutes, each time with an accelerating voltage of 1kV and an emission current of 10 mA. The resulting spectra are shown in the Figure S7. After sputtering the surface of 2D Ca₂N, we used XPS to determine the relative content of carbon (Fig. S7a), platinum (Fig. S7b), calcium (Fig. S7c), and nitrogen (Fig. S7d). We found that the carbon content decreased as sputtering time increased and that the calcium and nitrogen content increased. This is consistent with the removal of hydrocarbons from the surface of 2D Ca₂N. Furthermore, the unchanged position and shape of the calcium and nitrogen peaks after the sputtering indicated that we are not changing or damaging our material during the sputtering process. Additionally, this verifies that the film is generally thicker than the escape depth of the electrons since peaks from the Pt substrate (Fig. S7d) are barely detectable. Furthermore, the density of states up to the Fermi edge (Fig. S7e) becomes more prominent as hydrocarbons are removed from the surface of our thick film. Because XPS probes even deeper into the sample than UPS, we are confident that the density of states at the Fermi edge probed in our UPS measurements are exclusively attributable to the film of 2D Ca₂N and not the substrate.

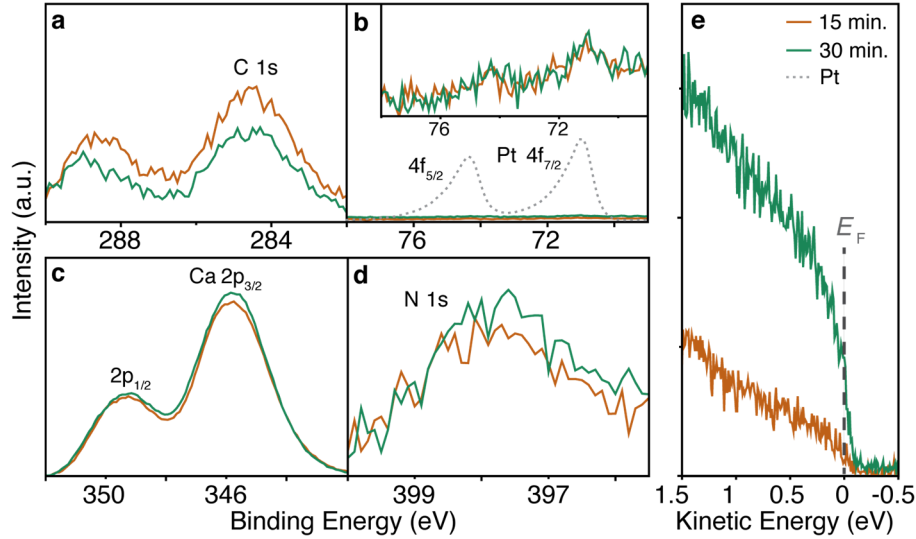


Figure S7. Photoemission spectroscopy of a thick film of 2D Ca_2N on a platinum-coated silicon wafer. After sputtering the film with argon ions to remove surface contamination, the film was characterized. In XPS, (a) the carbon content on the surface of 2D Ca_2N decreased as sputtering time increased from 15 minutes (orange) to 30 minutes (green). (b) The Pt film is almost entirely covered by Ca_2N , as shown by the extremely small peaks at 71.1 and 74.4 eV. The dashed line shows the positions of a bare Pt substrate; the intensities of the dashed line were reduced by a factor of 30. The inset shows a magnified version of the intensities for the Pt core electron binding energies on the film with 2D Ca_2N , showing that the Pt signal does not increase with sputtering time. (c) The calcium and (d) nitrogen peaks increase in area as hydrocarbons are removed by sputtering. (e) In UPS measurements, as hydrocarbons are removed, the density of states at the Fermi edge become more prominent and provides evidence for the metallic character of 2D Ca_2N .

Generally, UPS allows for calculation of the work function ϕ of a material. The work function is related to the Fermi energy of the instrument E_F , the energy of the incident photon $h\nu$, and the lowest kinetic energy at which electrons are emitted, E_{SECO} :

$$\phi = h\nu - (E_F - E_{\text{SECO}})$$

For conductive homogenous samples in electrical contact with the sample holder, the kinetic energy shifts exactly with the biasing potential; however, if different areas of the sample have different electrical conductivity or photoionization cross sections, then the areas of the sample have different steady-state potentials and some features only shift by a fraction of the biasing potential.²¹ We find that the surface of Ca_2N experiences this effect, which is called differential charging. As shown in Figure S8a, the XPS spectra of Ca 2p core electrons with the charge neutralizer active shows an additional feature that is not present in the spectra when the charge neutralizer is off; this is evidence of differential charging. Similarly in UPS, differential charging affects the secondary electrons emitted and prevents an accurate work function from being measured. The secondary cutoff electron edge E_{SECO} of 2D Ca_2N corrected by the applied bias, shown in Figure S8b, have a secondary feature that is induced with increasing applied biases. In Figure S8c, the work functions extracted from Figure S8b are plotted against the applied bias. The slope of the line ($\Delta \phi / \Delta \text{bias}$) varies between samples, but in all cases is much less than 1, which suggests that the sample exhibits differential charging. Unfortunately, this also indicates that we cannot extract a reliable work function from the surface of the material because the energy of the

secondary electrons are dependent on the applied bias and the degree of differential charging each sample experiences. We tested other metals (eg. Au, Pt) with known work functions and did not observe differential charging. Therefore, we believe that this response is from the Ca₂N sample and not an artefact of the instrument.

While this response could be caused by poor electrical contact between the sample holder and the drop-cast film, we think that this explanation is unlikely because our observation is consistent over many samples and the same observation was made on 3D Ca₂N in two other studies.^{1,22} As suggested by others,²² the response may be related to the highly anisotropic character of the samples that have areas of markedly different work functions.

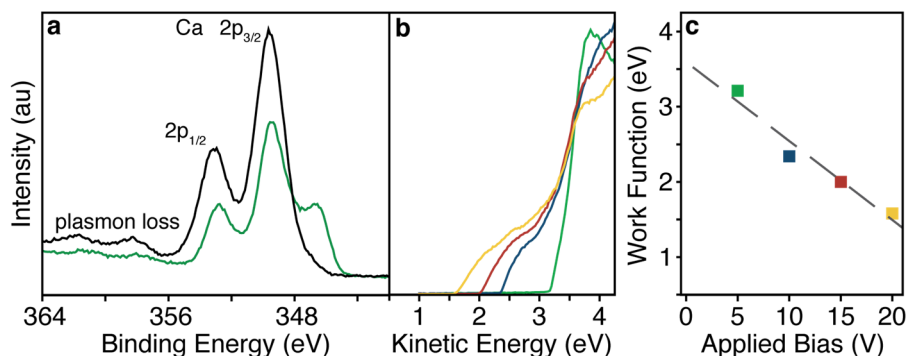


Figure S8. Differential charging of samples of 2D Ca₂N. a) XPS spectra of bulk Ca₂N Ca 2p electrons with the charge neutralizer on (green) and with the charge neutralizer off (black). b) UPS spectra of bulk Ca₂N with 5V (green), 10V (blue), 15V (red), and 20V (yellow) applied biases at the secondary cut-off energy, E_{SECO} . The spectra are corrected to account for the different applied biases. (c) Work function, ϕ , plotted against the applied bias for one sample of 2D Ca₂N.

7. Optical Response of 2D Ca₂N

We measured the optical response of 2D Ca₂N with UV-visible-near IR ($\lambda = 280\text{-}2200$ nm) transmission spectroscopy using a Cary 5000 double-beam spectrometer with an external integrating sphere attachment. Quartz cuvettes (Starna 1 mm path length) were filled with suspensions of 2D Ca₂N in 1,3-dioxolane in a glovebox and sealed with parafilm to maintain the N₂ atmosphere during the measurement. The attenuation of light through the sample depended linearly on sample concentration across all measured wavelengths (Figure S9).

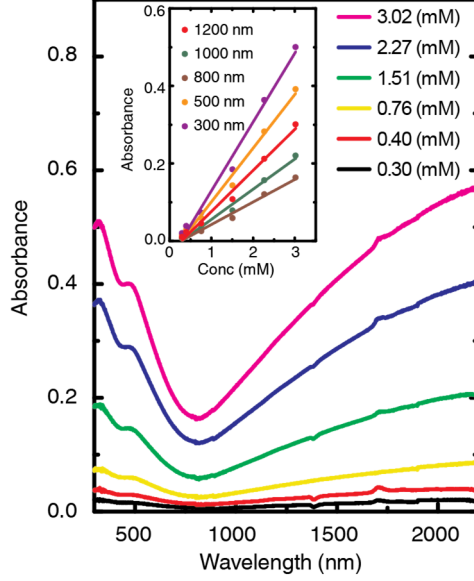


Figure S9. The absorbance of suspensions of 2D Ca₂N vs wavelength. The solvent has been background subtracted. The inset shows that the absorbance depends linearly on the concentration across the UV-Vis-IR range.

Previously reported reflectivity data for 3D Ca₂N¹ yielded a fit to the Drude-Lorentz model, which resolved one Drude component, described by a plasma frequency, ω_p , of 2.78 eV and mean scattering time, τ , of 0.64 ps, and two Lorentz components at 2.39 and 3.37 eV.

$$\omega_p^2 = \frac{Ne^2}{m_o \epsilon_o} \quad (1)$$

The Drude susceptibility, χ_D , described by ω_p and a damping factor $\gamma = \frac{1}{\tau}$ (Equation S2), primarily accounts for intra-band absorbance of free-carriers.

$$\chi_D(\omega) = \frac{-\omega_p^2}{(\omega^2 + i\gamma\omega)} \quad (2)$$

The Lorentz contribution χ_{Lj} , described by an oscillator frequency ω_j and damping factor γ (Equation S3), accounts for inter-band transitions.

$$\chi_{Lj}(\omega) = \frac{\omega_p^2}{(\omega_j^2 - \omega^2 - i\gamma\omega)} \quad (3)$$

The fit can be used to calculate the dielectric function $\epsilon(\omega)$ (Equation S4), which is related to the imaginary part of the refractive index, k .

$$\epsilon(\omega) = 1 + \chi_D(\omega) + \sum_{j=1}^n \chi_{Lj}(\omega) \quad (4)$$

$$\epsilon(\omega) = \epsilon_1(\omega) + i\epsilon_2(\omega) \quad (5)$$

$$k(\omega) = \frac{1}{\sqrt{2}} \left(-\epsilon_1(\omega) + \sqrt{\epsilon_1(\omega)^2 + \epsilon_2(\omega)^2} \right)^{\frac{1}{2}} \quad (6)$$

$$\alpha = \frac{2k\omega}{c} \quad (7)$$

The attenuation coefficient α (Equation S7), which is reported in Figure 4b, can be calculated by from k , the frequency of light ω , and the speed of light c .²³

The fit shows local maxima in attenuation at 360 nm and 520 nm in agreement with the JDOS and our experimental data. The magnitude of the attenuation coefficient predicted by the Drude-Lorentz model only differs from that of our 2D flakes by a factor of three. We note that because the reflectivity data used to make the fit to the Drude-Lorentz model only measured to 350 nm as a high energy bound, the damping term that describes the higher energy Lorentz component is subject to error; as a result, we believe that the attenuation coefficient calculated from this fit is likely overstated at 360 nm.

In addition, we compared our data to the JDOS of Ca₂N calculated from the band structure (Figure S10a). The JDOS accounts for direct transitions from unfilled states to filled states as illustrated by dark blue arrows. Interestingly, transitions from the flat band around -1.7 eV to the unfilled states in the conduction band constitute a large portion of the total JDOS (Figure S10b).

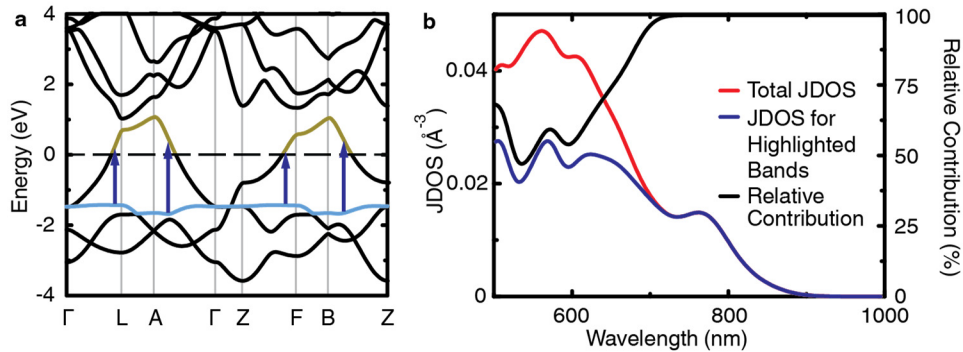


Figure S10. a) The band structure of Ca₂N highlighting the flat band of states with energies of -1.72 eV to -1.5 eV (blue) and the unfilled states in the conduction band with energies 0 eV to 1.00 eV (gold). Dark blue arrows depict direct transitions from the flat band to the conduction band. b) The joint density of states (JDOS) for the entire band structure (red) and for only the transitions from the flat band to the conduction band (dark blue). The relative contribution of those transitions to the total JDOS is given in black.

The experimental near IR data shows attenuation at wavelengths longer than 800 nm (Figure 4b). Because our experiment measures the transmittance of light, the attenuation is a combination of light scattering and absorbance despite our attempts to minimize the scattering component by

using an integrating sphere. To try to qualitatively understand whether the long-wavelength response is dominated by scattering or absorbance, we measured the transmittance with 1-cm quartz cuvette inside the integrating sphere and at the front of the integrating sphere (Figure S11). The wavelength was only measured to 1600 nm because the solvent, 1,3-dioxolane, absorbs too strongly in the NIR with a 1-cm cuvette to yield measurable signals.

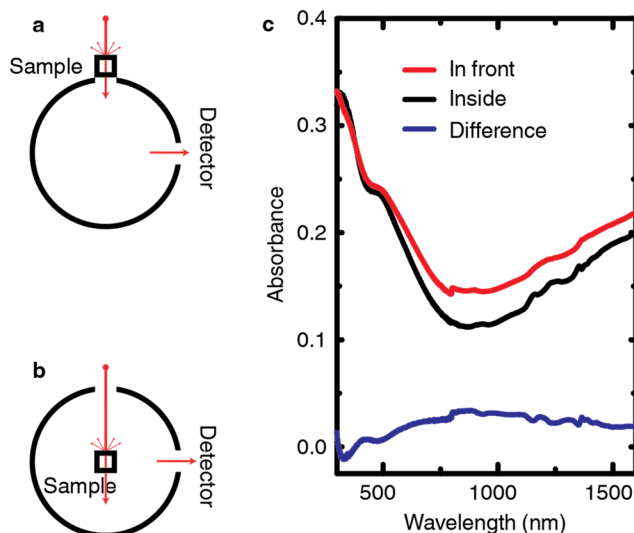


Figure S11. Schematic of the measurement with the sample a) in front of the integrating sphere and b) inside of the integrating sphere. The UV-vis-NIR absorbance spectra of Ca_2N vs wavelength with the sample in different geometries. The solvent has been background subtracted.

The Drude-Lorentz model predicts a minimum in effective attenuation around 800 nm in excellent agreement with our data. In the Drude-Lorentz model, the impinging light is either scattered from the surface or attenuated by electron scattering events inside of the particle. Because our particles have a high surface area to volume ratio, we expect electron surface scattering to decrease the mean scattering time, τ relative to bulk samples (0.64 ps).¹ Therefore we expect greater attenuation in our 2D Ca_2N . Still, a much smaller τ on the order of 1 fs or smaller would be needed to fit our data to the observed shape and we think that such a small relaxation time is unphysical.

The long-wavelength response could be due to overlapping plasmonic signals from the broad distribution of particle shapes and sizes. However, our measurements seem insensitive to the distribution of particle shapes and sizes. Without controlling for the size and shape of the particle and even with centrifuging at different speeds the long-wavelength response is consistent in all measurements. Therefore, the near IR response could have contributions from Drude absorbance and plasmonic signals. Further studies are needed to understand the long-wavelength response.

8. Supporting References

1. Lee, K.; Kim, S. W.; Toda, Y.; Matsuishi, S.; Hosono, H. *Nature* **2013**, *494*, 336.
2. Reckeweg, O.; DiSalvo, F. J. *Solid State Sci.* **2002**, *4*, 575.
3. Gregory, D. H.; Bowman, A.; Baker, C. F.; Weston, D. P. *J. Mater. Chem.* **2000**, *10*, 1635.
4. Clark, S. J.; Segall, M. D.; Pickard, C. J.; Hasnip, P. J.; Probert, M. I.; Refson, K.; Payne, M. C. *Z. Kristallogr.* **2005**, *220*, 567.
5. Kresse, G.; Furthmüller, J. *Phys. Rev. B* **1996**, *54*, 11169.
6. Vanderbilt, D. *Phys. Rev. B* **1990**, *41*, 7892.
7. Perdew, J. P.; Yue, W. *Phys. Rev. B* **1986**, *33*, 8800.
8. Grimme, S. *J. Comput. Chem.* **2006**, *27*, 1787.
9. Monkhorst, H. J.; Pack, J. D. *Phys. Rev. B* **1976**, *13*, 5188.
10. Oh, J. S.; Kang, C.; Kim, Y. J.; Sinn, S.; Han, M.; Chang, Y. J.; Park, B.; Kim, S. W.; Min, B. I.; Kim, H. *J. Am. Chem. Soc.* **2016**, *138*, 2496.
11. Morris, A. J.; Nicholls, R.; Pickard, C. J.; Yates, J. *Comp. Phys. Comm.* **2014**, *5*, 1477.
12. Pickard, C. J.; Payne, M. C. *Phys. Rev. B*, **1999**, *7*, 4685.
13. Pickard, C. J.; Payne, M. C. *Phys. Rev. B*, **2000**, *7*, 4383.
14. Guan, S.; Yang, S. A.; Zhu, L.; Hu, J.; Yao, Y. *Sci. Rep.* **2015**, *5*, 12285.
15. Yi, S.; Choi, J.; Lee, K.; Kim, S. W.; Park, C. H.; Cho, J. *arXiv preprint arXiv:1606.09347* **2016**.
16. Zhao, S.; Li, Z.; Yang, J. *J. Am. Chem. Soc.* **2014**, *136*, 13313.
17. Stadelmann, P. JEMS - EMS, Java version; <http://www.jems-saas.ch/>.
18. Patton, J.; Reeder, W. **1956**, *28*, 1026.
19. Searle, P. L. *Analyst* **1984**, *109*, 549.
20. Miller, D.; Biesinger, M.; McIntyre, N. *Surf. Interface Anal.* **2002**, *33*, 299.
21. Pertsin, A.; Pashunin, Y. M. *Appl. Surf. Sci.* **1990**, *44*, 171.
22. Steinbrenner, U.; Adler, P.; Hölle, W.; Simon, A. *J. Phys. Chem. Solids* **1998**, *59*, 1527.
23. Fox, M. *Optical properties of solids*; Oxford university press: 2010; Vol. 3.